

Fine-structure infrared lines from the Cassiopeia A knots

D. Docenko^{1,2} and R.A. Sunyaev^{1,3}

¹ Max Planck Institute for Astrophysics, Karl-Schwarzschild-Str. 1, 85741 Garching, Germany

² Institute of Astronomy, University of Latvia, Raiņa bulvāris 19, Rīga LV-1586, Latvia

³ Space Research Institute, Russian Academy of Sciences, Profsoyuznaya 84/32, 117997 Moscow, Russia

Preprint online version: November 2, 2018

ABSTRACT

Aims. Archival observations of the infrared fine-structure lines from the young Galactic supernova remnant Cassiopeia A allow to test existing models and to determine the physical parameters of various regions of the fast-moving knots – metal-dominated clouds of the material ejected in the supernova explosion.

Methods. The fluxes of the far-infrared [O I] and [O III] lines are extracted from the previously unpublished archival ISO data. The archival *Spitzer* data are used to determine the fluxes of the O, Ne, Si, S, Ar and Fe ion fine-structure lines originating in the fast-moving knots. The ratios of these line fluxes are used for the plasma diagnostics. We also determine the infrared line flux ratios to the optical [O III] 5007 Å line in the knots having previously measured reddening.

Results. We show that the infrared oxygen line flux predictions of all existing theoretical models are correct only to within a factor of several. Comparison of the model predictions shows that to reproduce the observations it is essential to include the electron conductivity and effects of the dust. Detailed analysis of the diagnostic line flux ratios of various ions allows us to qualitatively confirm the general model of the FMK emission and to determine observationally the physical conditions in the photoionized region after the shock front for the first time. We infer from the [O III] line flux ratios that the pre-shock cloud densities are higher than assumed in the existing theoretical models and most probably constitute several hundred particles per cm³. We determine also the Cas A luminosities in the infrared continuum and lines.

Key words. atomic processes - ISM: supernova remnants - infrared: ISM

1. Introduction

The young Galactic supernova remnant Cassiopeia A (Cas A) is one of only a few objects where the inner composition of the supernova progenitor may be studied directly, as the explosion ejecta have not yet mixed with the surrounding medium. In places where these ejecta are being crossed by the reverse shock wave, they are observable as compact knots emitting optical forbidden lines of ions of oxygen, sulphur, argon and other elements. Due to their high density, such ejecta knots are not strongly decelerated by the reverse shock wave and, as a result, have high proper motions, that motivated to name them as the fast-moving knots (FMKs). Studies of Peimbert & van den Bergh (1971) and Chevalier & Kirshner (1978, 1979) have firmly established that the FMKs are an observational manifestation of the supernova ejecta.

In the FMKs we therefore deal with very unusual situation in astrophysics where oxygen comprises 80%-90% of all atoms in the plasma, other components being mostly Ne, Si, S, Ar and Fe. The hydrogen and helium abundances are, in contrast, thought to be negligibly low. Optical observations have shown that some knots consist even of essentially pure oxygen (so-called [O III] filament, Chevalier & Kirshner (1979)).

Theoretical interpretation of the optical observations has proven that the plasma heated up to temperatures of several million degrees is rapidly cooling due to its high density and anomalous chemical composition of the gas. At the same time the ionization degree is lagging behind the rapid cooling rate. This results in a unique situation where atoms with strongly different ionization degrees coexist at low temperatures from 10⁴ K to several hundreds Kelvin. Just because of that, as we show be-

low, the lines of highly-charged ions, such as [Si x] and [Ar v], originate at temperatures about 10⁴ K and lower¹.

Traditionally, theoretical models of the fast-moving knot emission were compared only with the optical line observations. As there is only a very limited number of informative line ratios in the optical spectrum, the FMK theoretical models are both difficult to construct and to compare with optical observations. Most well-known models are the ones constructed by Itoh (1981a,b); Borkowski & Shull (1990) and Sutherland & Dopita (1995).

Recent paper by Docenko & Sunyaev (2008) has shown one way to constrain the theoretical models using prospective observations of the optical and near-infrared recombination lines of highly-charged oxygen ions.

In this paper we demonstrate how the existing archival infrared observations can discriminate between the existing models and set strong constraints for the construction of the future ones. We compare the model predictions of the far-infrared (FIR) fine-structure oxygen line flux ratios to the flux in the optical [O III] 5007 Å line with their observational values and show that all of the predictions are in error by a factor of several for one or several flux ratios. It should be remembered, however, that the theoretical models predict the deviations of ionic abundances from their collisional equilibrium values by orders of magnitude. Therefore inconsistencies of the observed order suggest that some corrections should be applied to the existing models,

¹ The [Si x] line has been detected also in spectra of several active galactic nuclei (Thompson 1996; Riffel et al. 2006), where it is apparently formed in the photoionized region. Even so, the models predict the line-forming region temperatures around 10⁵ K (Ferguson et al. 1997).

while the general picture described in the models is entirely correct.

The infrared fine-structure line flux ratios of other element (in addition to oxygen) ions are currently the best tool available for direct studies of the physical parameters in the FMKs. We made an attempt to estimate these parameters using available observational data. As a result, parameters of the post-shock photoionized region are estimated observationally for the first time, confirming qualitatively the predictions of the theoretical models, but again showing some quantitative differences.

The FIR lines will be even more important probe in future, as several far-infrared observatories, such as Herschel Space Observatory and SOFIA, will start their operation soon. They will provide much better FIR data with higher sensitivity and angular resolution, allowing to further constrain the FMK models.

Results of this study are important also for better understanding of the small-scale structure of other oxygen-rich supernova remnants, such as Puppis A, N132D, G292+1.8, etc.

The paper structure is following. In the next Section we briefly describe the existing theoretical models of the FMKs and estimate oxygen infrared line fluxes from one of them. Section 3 is devoted to description of the archival infrared observations of the Cas A and their analysis. In Section 4 we estimate the physical conditions and abundances in the different regions of FMKs from the observed line flux ratios. In Section 5 we discuss these results and compare them with the values predicted by the models. Finally, in Section 6 we conclude the article.

2. Theoretical models of the fast-moving knots

The first detailed model of a fast-moving knot emission, describing it as arising in the passage of a shock wave through the pure oxygen medium, was constructed by Itoh (1981a,b). His model H results were compared with the [O III] filament optical spectrum in the northern part of the Cas A supernova remnant (SNR) shell and reproduced all four measured oxygen [O I], [O II] and [O III] optical line flux ratios to within a factor of two. The infrared line ratios to the [O III] 5007 Å line² for this theoretical model (denoted I-H) and other models described below are given in Table 1.

In this and other theoretical models, the rapidly cooling region just after the shock front produces high flux of the ionizing radiation that results in appearance of two photoionized regions (PIRs): before and after the shock front (see Figure 1).

Later, Itoh (1986) discussed that the model neutral oxygen optical line intensities arising in the PIR after the shock front are much too high when compared to the observed spectra of the oxygen-rich supernova remnant Cas A and Puppis A ejecta. He suggested that emission from this region is damped because the region itself is truncated due to some hydrodynamical phenomena. It affects essentially only neutral oxygen lines, as all the other ions have already recombined in the dense post-shock plasma before reaching the photoionized region. This possibly makes the [O I] lines least reliable for direct comparison with model predictions, as all existing models are one-dimensional.

Another group of theoretical FMK models was proposed by Borkowski & Shull (1990). In contrast to the Itoh models, some

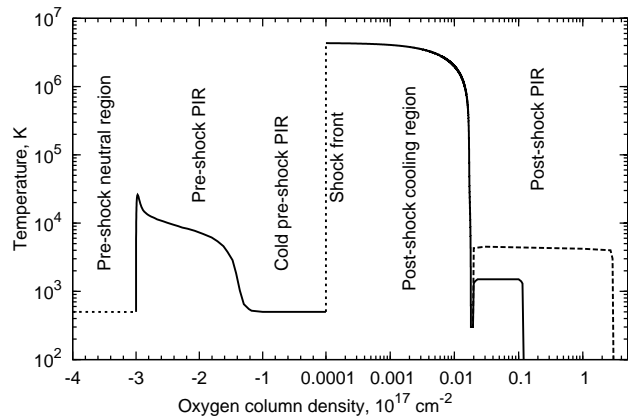


Fig. 1. Schematic representation of the FMK temperature structure, induced by its interaction with the reverse shock. Negative column densities corresponding to the pre-shock regions are in linear scale; positive (post-shock) column densities are in logarithmic scale. The post-shock photoionized region (PIR) parameters are given as derived in Section 5.2 (solid line) and according to the Borkowski & Shull (1990) models (dashed line). Shock is moving to the left. Due to the FMK high density the reverse shock in it is slowed down to about 200 km/s.

of them accounted for the electron conductivity that changed the line fluxes considerably. One more difference is that the Borkowski & Shull (1990) models do not account for the emission from the PIR before the shock wave. The models best describing the Cas A FMK optical spectra are F and DC (respectively, denoted as BS-F and BS-DC in Table 1 and below). Note that only the BS-DC model takes into account the electron conductivity.

Both Itoh (1981a,b) and Borkowski & Shull (1990) describe the emission arising in the pure oxygen plasma. However, it was shown by Dopita et al. (1984) that inclusion of other elements in the model significantly changes the plasma thermal structure and emission, especially in the cold PIRs, where a number of fine-structure transitions in ions of other elements can effectively cool plasma to temperatures of about one hundred Kelvin. Following this line of reasoning, another group of the FMK models was published by Sutherland & Dopita (1995). It describes emission arising in the interaction of the dense cloud with the external shock wave, entering the cloud and propagating through it. The expected far-infrared line intensities are not published and we estimate them in the Section 2.1 and 2.2 for the model with 200 km/s shock speed and pre-shock ion number density of 100 cm^{-3} (denoted as SD-200 in Table 1 and below), that is best reproducing the optical spectra of Cas A fast-moving knots, as demonstrated by Sutherland & Dopita (1995).

As compared to the models of Itoh (1981a,b) and Borkowski & Shull (1990), the SD-200 model does not include the PIR after the shock front, as it is constructed to describe the FMK optical spectrum and the temperature of this post-shock PIR is estimated to be too low to contribute significantly to the optical line emission.

All described models nevertheless share a lot of similar features (see Figure 1). In all of them the plasma after the shock front passage is rapidly cooling and, at temperatures of $(5-50) \times 10^3 \text{ K}$, emitting the high-ionization lines observable in the visi-

² The 5007 Å line is three times brighter than the other [O III] doublet component at 4959 Å (e.g., Osterbrock & Ferland (2006)). Note that in some papers the line intensities are compared to the sum of the doublet components.

Table 1. Far-infrared line flux ratios to the dereddened 5007 Å line as derived from different theoretical models and observations. See text for details.

$\lambda, \mu\text{m}$	$I/I(5007)$					f_{PIR} SD-200*
	I-H	BS-F	BS-DC	SD-200*	Observed**	
[O IV] 25.91	0.0051	5.0	0.53	8.1	0.20	0.995
[O III] 51.81	0.031	1.34	0.72	0.67	0.25	0.999
[O I] 63.19	1.30	170	12	—	0.07	—
[O III] 88.36	0.028	0.22	0.11	0.55	0.10	0.999
[O I] 145.5	0.038	7.8	0.75	—	<0.0024	—

* Derived in Sections 2.1 and 2.2.

** Obtained in Sections 3.1 and 3.2.1.

Notes. The last column lists contribution to the line flux in the SD-200 model arising from the photoionized region (PIR) before the shock wave. Derivation of the observed line flux ratio values is described in Section 3. The model-predicted [O I] lines are sensitive to the pre-shock ion number density in the model, see Section 4.1.2.

ble and near-infrared spectra (Chevalier & Kirshner 1978, 1979; Hurford & Fesen 1996; Gerardy & Fesen 2001). Thickness of this emitting layer is extremely small (about 10^{10} cm for the pre-shock ion density of 100 cm^{-3}), but due to the high electron density in the cooling material at $T < 10^5$ K (more than 10^5 cm^{-3}) the emission measure is enough to produce or contribute to bright emission lines of highly-charged ionic species, such as [O III] lines near 5000 Å.

In all these models the visible line emission of weakly-ionized ionic species (e.g., [O I] and [O II]) is arising in photoionized regions before and after the shock front.

Although all of the theoretical models describe optical spectrum relatively well, with discrepancies in relative intensities not exceeding factors of about two, predictions for the infrared lines differ by several orders of magnitude (see Table 1). It is therefore clear that the models have lack of constraints and more diagnostic information in form of various line flux ratios is needed to pin down the true structure of the fast-moving knots. Part of such information may be obtained from the far-infrared line archival observations, and we present such analysis in the Section 3 below.

2.1. Infrared lines from the SD-200 model

Because of lack of published values, we had to make our own estimates of the far-infrared line fluxes and their ratios to the [O III] 5007 Å line in the SD-200 model. Fortunately, all the data necessary for such calculation – ionic abundances of all oxygen ions, temperature and density structure of the post-shock region and temperature structure of the pre-shock photoionization front – are known for the SD-200 model³.

Note that the FMK structure calculations in the SD-200 model are based on the plasma composition that is slightly different from the composition inferred from the X-ray and optical observations. Specifically, it is dominated by O (63% by number) and Ne (29%) and contains minor amounts of C, Mg and Si. In contrast, the observations show that the major part of the

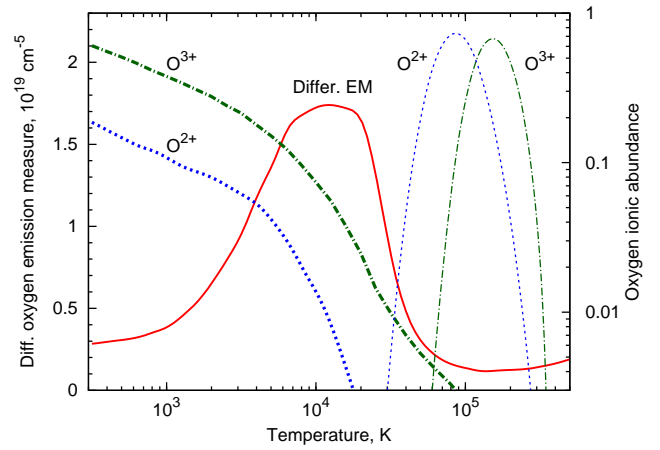


Fig. 2. Comparison of ionic abundances of oxygen ions O^{2+} and O^{3+} in the collisional ionization equilibrium (thin curves) and in the cooling post-shock region of the SD-200 model (thick curves of the same color). The differential oxygen emission measure per logarithmic temperature interval $dE_O/d \log T_e$ is shown with the red solid line.

currently bright X-ray and optical plasma contains about 90% of oxygen with other abundant elements being not only Ne, but also Si and S.

On Figure 2 we demonstrate how strongly different is the ionization state distribution in the SD-200 model as compared to the collisional ionization equilibrium (CIE, Mazzotta et al. (1998)) on examples of the O^{2+} and O^{3+} ions producing bright FIR lines. It is seen that in the rapidly cooling plasma these ions are abundant at significantly lower temperatures (down to 300 K and below) than in the CIE due to very rapid plasma cooling via the line emission.

On the same figure we present the oxygen ion emission measure distribution over temperature $dE_O/d(\log T_e)$ in the SD-200 model, defined in Equation (3). This distribution together with the line emissivity dependence on temperature allows one to calculate the relative contributions to the total line flux from different temperature intervals (see Section 2.2).

³ We made our own computations of the post-shock plasma recombination and discovered that our oxygen ion distribution over ionization stages is rather similar to the one presented on the lower panel of Figure 3 of the Sutherland & Dopita (1995), but only if the ion spectroscopic symbols on that figure are increased by unity. Therefore we assume that the Figure 3 of Sutherland & Dopita (1995) has a misprint and the ion spectroscopic symbols should be read, e.g., “O VII” instead of “O VI”, “O VI” instead of “O V”, etc. Therefore, the SD-200 model values for the neutral oxygen abundances are not known and we do not provide estimates of the FIR [O I] line intensities.

2.2. Line flux computation

The emissivity, cm^3/s , of a spectral line corresponding to transition from level u to level l is defined as

$$\varepsilon(u, l) = n_u A_{ul} / n_e n_i, \quad (1)$$

where n_e , n_i and n_u are the number densities of electrons, corresponding ionic species and ions in the state u , respectively, and A_{ul} is the spontaneous $u \rightarrow l$ transition rate.

For oxygen ions at temperatures above 1000 K the line emissivities ε were obtained from the CHIANTI atomic database (Dere et al. 1997; Landi et al. 2006). For lower temperatures and other ions, we have computed emissivities using a standard approach, i.e., calculating the level populations by solution of a system of linear equations describing transitions between the lowest ionic levels using electronic excitation effective collision strength data from literature and spontaneous transition rates from the Ralchenko et al. (2007) database⁴ and MCHF/MCDHF collection⁵, and then applying Eq. (1) to derive the line emissivities.

The electronic collisional excitation effective collision strength values were taken from Dufton & Kingston (1991); Blum & Pradhan (1992); Zhang et al. (1994); Butler & Zeppen (1994); Lennon & Burke (1994); Galavis et al. (1995); Pelan & Berrington (1995); Berrington et al. (1998); Tayal & Gupta (1999); Griffin & Badnell (2000); Griffin et al. (2001); Tayal (2006) and Ramsbottom et al. (2007) and extrapolated to lower temperatures by a constant, if needed.

Line fluxes $I(u, l)$, $\text{erg}/\text{cm}^2/\text{s}$, were computed by integrating along the line of sight

$$I(u, l) = h\nu \frac{S}{4\pi R^2} \int \varepsilon(u, l; T_e(r)) n_e(r) n_i(r) dr, \quad (2)$$

where $h\nu$ is the photon energy, R is the distance from the observer to the emitting region (3.4 kpc, Reed et al. (1995)) and S is the emitting region area. From this expression it is seen that the line emission is mostly arising in regions having highest emission measure $n_e n_O dr$, ionic abundance n_i/n_O and emissivity ε (here n_O is the total number density of all oxygen ions).

The integral over distance in the post-shock cooling region can be easily transformed into integral over temperature by substitution

$$dr = \frac{dr}{dt} \frac{dt}{dT} dT = v_{\text{shock}} \frac{n_{0,t}}{n_t} \frac{3/2(n_t + n_e)k_B}{n_t n_e \Lambda_N} dT,$$

where v_{shock} is the shock front speed, Λ_N is the cooling function (Sutherland & Dopita 1993) and n_t and $n_{0,t}$ are the total number densities of all ions in plasma at a given point and before the shock (i.e., in the SD-200 model $n_{0,t} = 100 \text{ cm}^{-3}$). It is assumed here that the photon heating is insignificant compared to the energy losses. Parameters of this equation – cooling function, electron and ion densities as functions of temperature – were taken from the SD-200 model.

For purpose of qualitative analysis, we introduce the oxygen differential emission measure per logarithmic temperature interval

$$\frac{dE_O}{d(\log T_e)} = T_e \frac{n_O n_e dr}{dT_e}. \quad (3)$$

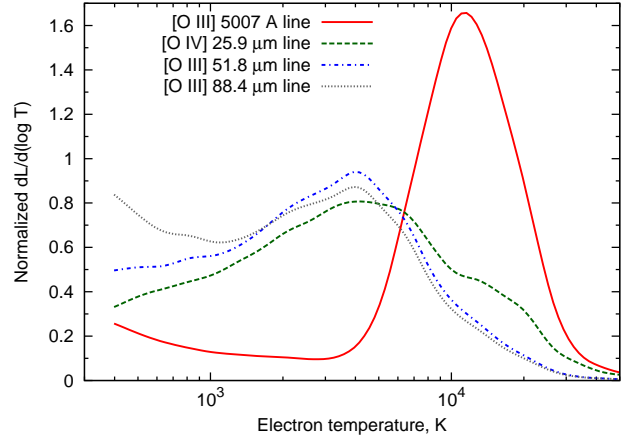


Fig. 3. Differential luminosity contribution per logarithmic temperature interval for the optical [O III] 5007 Å line and discussed infrared lines in the cooling post-shock region according to the SD-200 model. Curves are normalized so that the area enclosed under each of them equals one. Low-temperature (below 4000 K) contribution to the optical [O III] line is due to recombination.

It shows contribution of a given logarithmic temperature interval to the total emission measure, showing where most of the line emission originates. Using this notion, we can express the line flux from Eq. (2) as

$$I(u, l) = h\nu \frac{S}{4\pi R^2} \int \varepsilon(u, l; T_e) \frac{dE_O}{d \log T_e} \frac{n_i}{n_O} \frac{dT_e}{T_e}.$$

Contributions from different temperature intervals to the emission of the post-shock cooling region in the oxygen lines are illustrated on Figure 3, where we plot the normalized line luminosities per logarithmic temperature interval. It is seen that the post-shock contribution to the visible [O III] line emission is arising at temperatures of $(5-20) \times 10^3$ K, whereas the infrared lines are emitted mostly at lower temperatures. They also have much broader range of temperatures contributing to the line emission because of lower excitation energies.

In our analysis, we artificially stop integrating expression (2) in the post-shock region when the plasma temperature drops below 300 K, as the SD-200 model does not contain data for lower temperatures. This should not influence much the total FIR line intensities, as the model predicts them to be mainly emitted in the pre-shock region.

In the pre-shock PIR the ion density is constant and temperature dependence on time for the SD-200 model is known explicitly. Therefore the Eq. (2) was applied directly to compute the line fluxes from this region.

Resulting line flux ratios are given in Table 1.

3. Archival observations of the FIR lines

The first search for the [OI] 63.19 μm line was performed by Dinerstein et al. (1987), who observed the northern part of the Cas A using the NASA Kuiper Airborne Observatory. This search resulted in a $3\text{-}\sigma$ upper limit of reddening-corrected flux ratio $I(63.19 \mu\text{m})/I(5007 \text{ Å})$ of about 0.3, already constraining some theoretical models.

⁴ Available online at <http://physics.nist.gov/asd3>

⁵ <http://atoms.vuse.vanderbilt.edu/>

Later, the far-infrared lines of O, Ne, Si, S and Ar ions were detected by the Infrared Space Observatory (ISO, Arendt et al. 1999). We describe our analysis of some of these archival observations in Section 3.1.

Recently, the *Spitzer* Space Telescope has spectrally mapped this supernova remnant (Ennis et al. 2006; Rho et al. 2008). In Section 3.2, we determine the line ratios⁶ of O, Ne, Si, S, Ar and Fe lines to the [O III] 5007 Å line.

To determine these ratios, we compare the infrared observations of ISO and *Spitzer* with the optical images of the Hubble Space Telescope. The best method for comparison of these observations would be an analysis of the properties of individual knots but, unfortunately, the ISO data have insufficient angular resolution (about 40"). The angular resolution of the *Spitzer* data is much better (2"–8"), but also too coarse for isolating contributions of *individual* knots distinguishable on the optical maps (0.2–1", corresponding to $(3 - 15) \times 10^{16}$ cm at 3.4 kpc).

As the optical observations show, the bright FMK lifetime is of the order of 30 years (Kamper & van den Bergh 1976) that is determined by the time needed for the shock wave to cross the cloud. After that the knots fade, but other ones gradually appear on the maps of the Cas A. Therefore one may directly compare either observations performed with a small time difference between them (as it is the case with the Hubble Space Telescope observations compared with the *Spitzer* data), or averaged over large area (as it is the case with ISO data).

3.1. ISO observations

The Infrared Space Observatory⁷ Long Wavelength Spectrometer (ISO LWS) observations of the Cassiopeia A supernova remnant have been performed in 1996 and 1997. Here we do not discuss observations at shorter wavelengths ($\lambda < 40 \mu\text{m}$), as more recent data from the *Spitzer* observatory is available, having significantly higher angular resolution.

To determine the line fluxes, we used the ISO LWS calibrated data from a highly-processed data product “Uniformly processed LWS L01 spectra” available at the ISO data archive⁸.

There are seven LWS observations in L01 mode each covering full instrument spectral range between 43 and 170 μm with medium spectral resolution ($\lambda/\Delta\lambda$ between 150 and 200). The regions observed by ISO are shown on Figure 4 overlaid with the Hubble Space Telescope Advanced Camera for Surveys (HST ACS) Cas A image in filter F475W, containing [O III] 4959 and 5007 Å lines (Obs.ID 10286, observations made in December 2004, Fesen et al. (2006)).

The ISO LWS observational data are summarized in Table 2 and the spectral cuts containing the discussed lines are presented on Figure 5.

To compute the far-infrared spectral line fluxes, we subtracted the background continuum flux and averaged over three scans of the same detector weighting the data corresponding to its uncertainties. In case of the [O III] 88.36 μm line it was possible to estimate the systematic uncertainties by comparing the flux values obtained from two neighboring detectors. The flux differences are expected to be arising due to two reasons: slightly

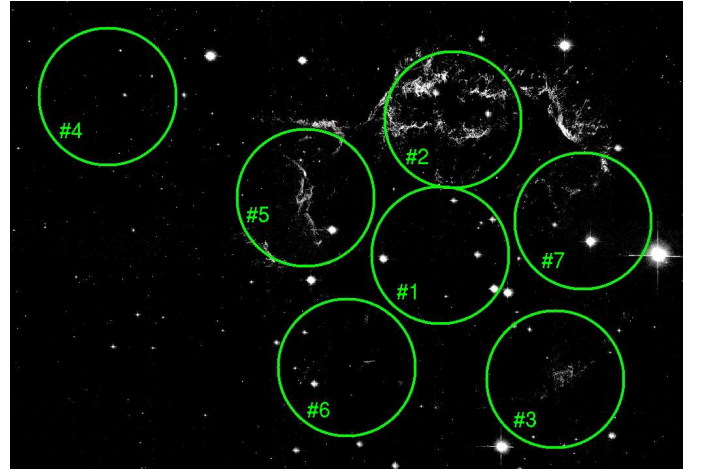


Fig. 4. ISO LWS apertures (green circles) overlaid on the Hubble Space Telescope 2004 ACS image of Cas A in F475W filter (Fesen et al. 2006). North is upwards and East is to the left.

Table 2. Summary of the ISO LWS archival observations of the Cassiopeia A.

ID	Date	Exposure	R.A.	Dec.
Cas A #1	1996 Jun 24	1054 s	350.8656	+58.8130
Cas A #2	1996 Jun 24	1052 s	350.8614	+58.8361
Cas A #3	1996 Jun 24	1054 s	350.8279	+58.7919
Cas A #4	1996 Jun 24	1054 s	350.9748	+58.8400
Cas A #5	1997 Jun 09	1612 s	350.9097	+58.8228
Cas A #6	1997 Jun 09	1612 s	350.8963	+58.7939
Cas A #7	1997 Jun 02	1614 s	350.8186	+58.8188

different apertures of the detectors and systematic errors due to imperfect instrumental calibration (Gry et al. 2003). Our analysis showed that differences between the two detector measurements do not exceed 10–15%, when the line flux determination accuracy is sufficiently high (see Figure 5 for visual comparison).

The background-subtracted FIR line fluxes from the observed regions are presented in Table 3. It is seen that flux on the level of up to 10% of brightest fields is observed in the 88.36 μm from the region #4 situated outside the main supernova remnant shell and having no detected optical [O III] emission and very little diffuse emission in other optical bands. We consider the flux from this region as coming from foreground and/or background of the Cassiopeia A and in our analysis subtract it from the fluxes of other regions.

In the same table we give the total fast-moving knot optical flux in the matched regions in the F475W filter of the discussed HST ACS data. The diffuse emission in this filter is assumed to be coming only in the [O III] 4959 and 5007 Å lines.

From these data we have calculated the line ratios to the [O III] 5007 Å line, given in Table 4. Assuming that the FIR line emission observed by ISO is arising in the same spatial regions where the optical line emission originates, these flux ratios are characteristic for the knot emission and may be used for tests of the theoretical models. If significant large-scale diffuse emission in the FIR lines is present, like one observed in the [S III] and [O IV] lines from *Spitzer* observations (see Section 3.2), then the

⁶ Here and everywhere below the “line ratio” denotes the ratio of the line fluxes in energy units.

⁷ Results in this section are based on observations with ISO, an ESA project with instruments funded by ESA Member States (especially the PI countries: France, Germany, the Netherlands and the United Kingdom) and with the participation of ISAS and NASA.

⁸ <http://www.iso.vilspa.esa.es/ida/>

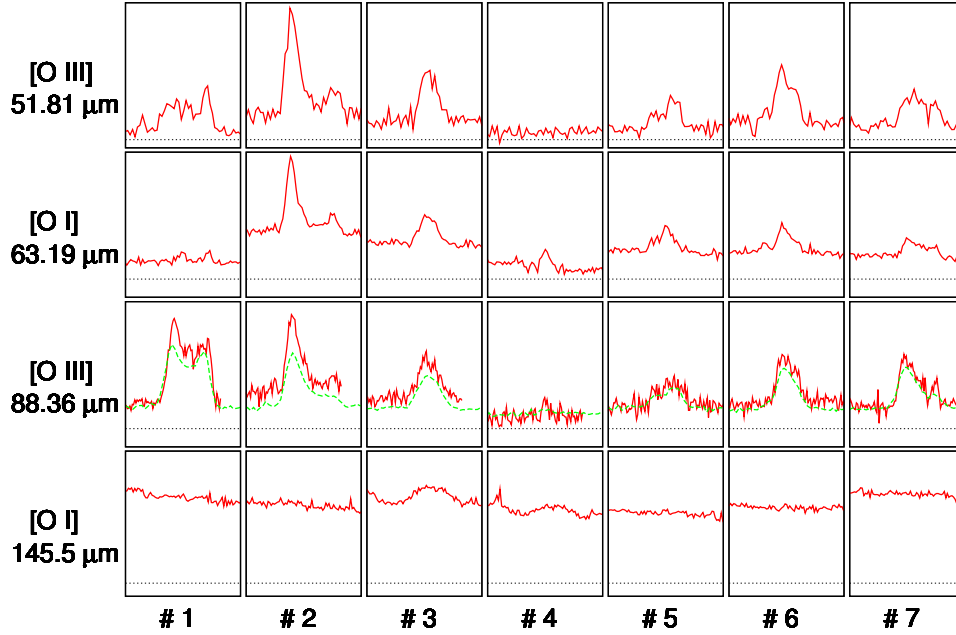


Fig. 5. ISO LWS spectral cuts containing oxygen far-infrared lines discussed in the text (averages over three scans weighted according to their uncertainties). Continuum emission is not subtracted. Two curves for the 88.36 μm line correspond to measurements by two different ISO detectors. The short-dashed line denotes zero level; maximum intensity corresponds to 1.7×10^{-10} , 0.7×10^{-10} , 0.7×10^{-10} and 0.10×10^{-10} $\text{erg/cm}^2/\mu\text{m}$ for [O III] 51.81 μm , [O I] 63.19 μm , [O III] 88.36 μm and [O I] 145.5 μm lines, respectively. Spectral ranges are centered on the rest wavelengths of the respective spectral lines and include velocity range of $\pm 10^4$ km/s.

Table 3. Far-infrared line fluxes from the ISO LWS observations of Cas A. Fluxes from the matched regions in the HST ACS F475W filter are also given. The upper limits are on the 3σ level.

Line	#1	#2	#3	#4	#5	#6	#7
FIR line fluxes F , 10^{-11} $\text{erg/cm}^2/\text{s}$							
[O III] 52 μm	5.4	9.3	5.4	<1.2	3.5	5.0	5.2
[O I] 63 μm	<0.6	2.6	1.2	<1.2	1.0	1.0	0.9
[O III] 88 μm	7.5	4.2	2.7	0.5	1.9	3.2	3.4
[O I] 145 μm	<0.1	<0.09	0.3	0.1	<0.1	<0.1	<0.1
[O III] 4959 + 5007 \AA line flux F , 10^{-13} $\text{erg/cm}^2/\text{s}$							
	<0.1	25	2.0	<0.1	6.5	0.5	2.9

Note. ISO region positions are shown on Figure 4. Regions #3, #6 and #7 have higher interstellar absorption column (Bieging & Crutcher 1986).

Table 4. Far-infrared line flux ratios to the optical 5007 \AA line $I/I(5007 \text{\AA})$ corrected for the optical line reddening.

Line	#2	#5
[O III] 51.81 μm	0.25	0.36
[O I] 63.19 μm	0.07	0.10
[O III] 88.36 μm	0.10	0.14
[O I] 145.5 μm	<0.0024	<0.01

Note. The 5007 \AA line contribution of 75% to the total FMK emission in the F475W filter is assumed. Optical line attenuation due to reddening of 200 times is assumed in both ISO LWS regions, see text. FIR line attenuation is neglected.

determined line ratios should be interpreted as the upper limits on the values characteristic for the knots.

In Table 4 we provide the values corrected for the interstellar absorption of the optical line using an average value from Hurford & Fesen (1996). This level of reddening diminishes observed visible [O III] doublet intensities by a factor of about 200 ($A_V \approx 5.0$) and is characteristic for region #2 and, possibly, region #5 (Bieging & Crutcher 1986).

For southern and eastern regions (#3, #6 and #7) the reddening is known to be much higher due to absorption in the molecular clouds with peak A_V 's reaching 10–15 (Bieging & Crutcher 1986) corresponding to the optical line attenuation up to factors of 10^4 and more. Therefore we do not provide dereddened line ratios in these regions. In our further analysis in Sections 4 and 5.4 we use only the data from the region #2.

There is an eight-year time difference between ISO and HST observations. During this time, which is about 30% of a bright FMK lifetime (Kamper & van den Bergh 1976), some optical knots may have disappeared, and new ones may have appeared. Though, averaging over large number of optical knots contained in any ISO LWS field of view at least partially cancels changes induced by brightening or fading of individual knots.

3.2. Spitzer Space Telescope observations

Recently, the *Spitzer* Space Telescope has spectrally mapped the Cassiopeia A in the infrared range using its Infrared Spectrograph (IRS) producing low-resolution spectra from 5 to 38 μm (Ennis et al. 2006; Rho et al. 2008) and detected in this spectral band the fine-structure lines of [O IV], [Ne II], [Ne III], [Ne V], [Si II], [S III], [S IV], [Ar II], [Ar III], [Ar V], [Fe II], etc.

We have used basic calibrated data of these publicly available *Spitzer* observations (Program 3310) to construct the data cube over all remnant with the CUBISM software (Smith et al. 2007). The background regions were determined from the $8\ \mu\text{m}$ MIPS images of the supernova remnant (Hines et al. 2004).

The line flux maps were then produced using the parabolic approximation for the background continuum emission. This allowed the maps to be constructed reliably even for the weak lines in the regions of strong continuum dust emission.

As the *Spitzer* spectral maps and the HST images were obtained almost simultaneously with a time difference of only one month, we could make a direct pixel-by-pixel comparison of the infrared line map with the optical image. For this purpose, we have processed the HST images: removed the stars, convolved with the point spread function (PSF) of a given *Spitzer* spectral map computed as described in Appendix A, and regridded the HST image to match pixels to the IRS module containing given infrared line. Such matched HST images were produced and compared to each of the infrared lines.

3.2.1. The oxygen [O IV] $25.91\ \mu\text{m}$ line

The [O IV] $25.91\ \mu\text{m}$ spectral line map of the northern Cas A shell region from *Spitzer* observations is presented on Figure 6. Alongside, we show the HST image in F475W filter processed as described above. The northern region is of primary importance as it has well-measured and almost constant interstellar absorption level.

It can be readily seen from the brightest features on the Figure 6 that there is a certain difference between the Cas A morphologies in optical and infrared lines. It may originate due to several reasons: variations of the interstellar reddening (Hurford & Fesen 1996), emitting plasma chemical composition (Chevalier & Kirshner 1979) and FMK pre-shock density distribution over the remnant.

On Figure 7 we present the resulting pixel-by-pixel scatter plot showing interrelation between the [O IV] infrared and [O III] optical line fluxes. From such comparison of the maps we derive the average line ratio between optical and infrared lines, corresponding to an average reddening, FMK density and chemical composition.

In this analysis, “average” reddening was assumed to diminish the observed optical [O III] line emission 200 times, that is an average of the Hurford & Fesen (1996) measurements. As may be inferred from their paper, the small-scale variations of the interstellar reddening in this region change the optical line attenuation within a factor of two. The observed scatter of the line ratio seen on Figure 7 is of similar magnitude.

On the same Figure we present also data on five FMKs having reddening measured by Hurford & Fesen (1996). Their positions are shown on Figure 7. In these cases, the reddening correction was made according to their measurement results. Four out of five points lie very close to the best fit lines, showing that considerable part of the FMKs have similar excitation conditions. Remaining point (FMK 1) have relatively weaker [O IV] emission, showing that the physical conditions there are different. This region (Filament 1 of Baade & Minkowski (1954)) indeed has composition different from other regions (Chevalier & Kirshner 1979).

On Figure 6 it is also seen that a noticeable infrared emission in the [O IV] line is arising in the central Cas A region having no optical nebulosity (see also Rho et al. (2008)). On Figure 7 such infrared-only emission shows up on the left as a horizontal branches, corresponding to an approximately constant

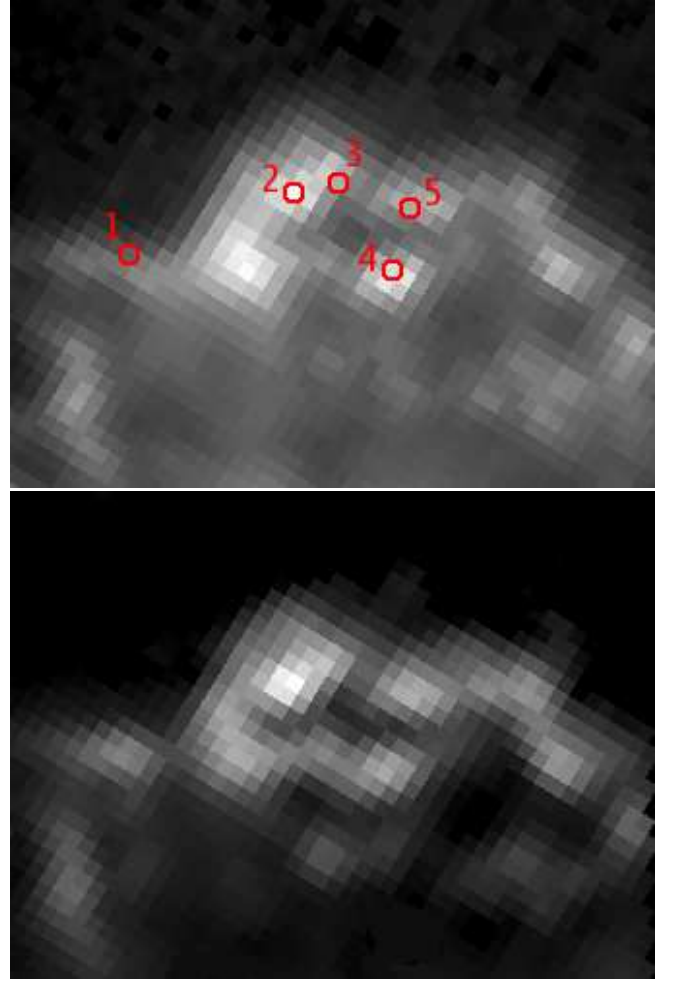


Fig. 6. The *Spitzer* Space Telescope map of the northern part of the Cas A optical shell rich in FMKs in the [O IV] line at $25.91\ \mu\text{m}$ (top) compared with the HST image in F475W filter matched in resolution and in pixels (bottom). The red circles denote regions having reddening measured by Hurford & Fesen (1996). Square root scale in intensity is used to enhance weak features. Diffuse infrared [O IV] emission from optically-dark regions is clearly visible.

background surface brightness. Two such branches are apparent, probably corresponding to two different column densities of the O^{3+} ion. Pixels forming the lower branch are situated just outside the optical shell, where the optical surface brightness is already fading, but the infrared line emission is still present.

The upper branch corresponds to the diffuse level emission in the central part of the supernova remnant. Corresponding points on the HST image are partially out of the Figure 7 plot range, but the infrared line surface brightness remains on the level of $(1 - 3) \times 10^{-13}\ \text{erg/cm}^2/\text{s/pix}$.

This infrared-only line emission hints on the existence of extended cold photoionized regions invisible in optical and X-ray emission near the center of the supernova remnant, possibly connected with the thermal radio absorption observed in the same regions (Kassim et al. 1995; Delaney 2004).

Note that the [O IV] infrared line at $25.91\ \mu\text{m}$ overlaps with the [Fe II] line at $25.99\ \mu\text{m}$, but contribution of the latter can be

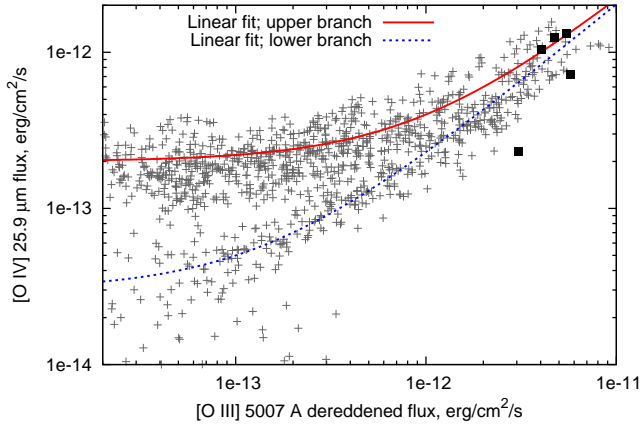


Fig. 7. Pixel-by-pixel comparison of the dereddened 5007 Å line flux with the infrared [O IV] line map. Fluxes are given per detector pixel, equal to $(5''.08)^2$ for the IRS LL module containing the infrared oxygen line. Two linear fits, both having the same slope of 0.20, are shown with lines. Filled squares denote FMKs from Hurford & Fesen (1996) having measured reddening.

estimated from the comparison with the [Fe II] 17.94 μm line map. Such estimates result in the upper limit on the 25.99 μm [Fe II] line contribution to the total flux of the observed line near 26 μm of 10 – 30% in all regions of the Cas A used for our further analysis. The energy considerations are discussed further in Section 3.2.3.

3.2.2. Other infrared lines in the *Spitzer* spectral maps

Similar pixel-by-pixel comparisons with the optical image have been performed also for other bright spectral line flux maps. In Table 5, we give the derived the flux ratios to the optical [O III] 5007 Å line in five Hurford & Fesen (1996) FMKs and average values of these ratios in the northern part of the Cas A shell. Last digit in brackets in the “Average” column denote observed scatter around the average line flux ratio.

From the table it is seen that different line flux ratios have different scatters around their average values. Small scatter in e.g. Ar, Si and S line ratios to the 5007 Å line corresponds to the Cas A morphology in these lines similar to the optical one. Larger scatter, present in e.g. Ne and Fe line ratios to the 5007 Å line corresponds to different morphologies of the infrared spectral maps, as noted also by Rho et al. (2008).

Obtained line ratios may be further used for tests of the theoretical models and are utilized in the next Section to estimate average abundances and physical conditions in the bright Cas A knots.

From the Table 5 it is seen that the full energy flux in the infrared lines detected by *Spitzer* exceeds one of the brightest optical line – [O III] 5007 Å – and is of the same order as the total power in all optical lines summed up.

3.2.3. Energetics of the infrared emission

From the analysis of the *Spitzer* archival observations it is straightforward to determine that in the wavelength range from 5 to 35 μm the total Cas A luminosity is 3.3×10^{37} erg/s (the

luminosity values are computed assuming a distance to Cas A of 3.4 kpc, Reed et al. (1995)). The total spectral line luminosity in the same range is found to be one order of magnitude smaller, contributing 3.0×10^{36} erg/s.

For the longer wavelengths between 35 μm and 1 mm we have estimated the total Cas A luminosity from data published by Hines et al. (2004) to be about 1.5×10^{37} erg/s. The line contribution to this value in the narrower ISO LWS range between 40 and 200 μm is about 9×10^{35} erg/s, as follows from Table 3. Therefore, the total Cas A dust continuum and line luminosities in the infrared range between 5 μm and 1 mm are respectively 4.7×10^{37} and 3.9×10^{36} erg/s.

It is interesting to compare these values with the X-ray and radio luminosities. In radio, the total luminosity at wavelengths longer than 1 mm is about 1.0×10^{35} erg/s that is calculated directly from the spectrum provided by Baars et al. (1977) and Hines et al. (2004), i.e., much lower than in the infrared.

It is not so straightforward to determine the total Cas A luminosity in X-rays because of interstellar and internal X-ray absorption. Various estimates result in values corrected for the absorption of $(1 - 5) \times 10^{37}$ erg/s (Hartmann et al. 1997; Zombeck 2007), but are dependent on the assumed spectral model and absorbing material column density.

It is seen from this comparison that the the infrared continuum emission is as important radiative energy loss mechanism from the supernova remnant as the X-rays. Note, however, that the energy contained in the Cas A infrared emission was originally emitted in far-ultraviolet and soft X-rays and then absorbed within the emitting knot (see Figure 1). Therefore, the infrared luminosity gives us a model-independent lower boundary on the total cooling plasma luminosity between 10 and 200 eV or so (photons of lower energies do not ionize oxygen; photons of higher energies have lower absorption cross-sections and escape from the dense knot).

It is easy to notice that the infrared line-to-continuum emission ratio in the *Spitzer* range is variable over the supernova remnant, as indicated also by the spectra provided by Rho et al. (2008), with a typical value of 0.10. The highest values of this ratio of about 0.22 are characteristic for the central Cas A region. In these regions, the energy losses in the line emission are relatively twice higher than on average, however, still staying significantly below the losses in the infrared continuum.

4. Physical conditions and abundances in the FMKs

The measured line fluxes may be directly used to determine the ionic abundances⁹, if the model of the emitting region (temperature and density distribution) is known. As the models do not reproduce observations precise enough (see Table 1), we cannot suppose that such distribution is known for the FMKs.

Thus the line fluxes cannot be used in such a direct fashion and the inferred ionic abundances will depend on the assumed physical conditions. Fortunately, emissivities of some of the fine-structure lines are only weakly dependent on the electron densities and temperatures in rather wide range, allowing to use these lines for the abundance determination even without detailed knowledge on the line-emitting region properties.

Analysis of the measured flux ratios of the lines of the same ion is a more powerful method. Such line ratios may be used

⁹ In this paper, by abundance we denote a ratio of number density of given ions or atoms to the number density of all oxygen ions (i.e., n/n_{O}).

Table 5. Infrared line fluxes I and their ratios $I/I(5007 \text{ \AA})$ to the dereddened optical [O III] 5007 \AA line from the *Spitzer* data. The column “Average” contains the ratio values averaged over northern part of the Cas A and their observed scatter, other columns contain data on the Hurford & Fesen (1996) FMKs.

Line	Line flux I , $10^{-13} \text{ erg/cm}^2/\text{s/pixel}$					Flux ratio $I/I(5007 \text{ \AA})$					
	FMK 1	FMK 2	FMK 3	FMK 4	FMK 5	Average	FMK 1	FMK 2	FMK 3	FMK 4	FMK 5
[Ar II] 6.985 μm	3.8	14	17	5.6	11	0.5(1)	0.41	0.75	1.15	0.46	0.79
[Ar III] 8.991 μm	0.46	2.0	1.7	0.80	1.5	0.08(3)	0.05	0.13	0.12	0.07	0.12
[S IV] 10.51 μm	0.24	1.6	1.4	0.67	0.91	0.07(2)	0.025	0.11	0.10	0.06	0.07
[Ne II] 12.81 μm	0.31	0.92	0.89	1.0	0.30	0.10(8)	0.04	0.07	0.07	0.08	0.025
[Ne V] 14.32 μm	0.071	0.20	0.18	0.10	0.14	0.012(7)	0.009	0.012	0.012	0.009	0.014
[Ne III] 15.56 μm	0.29	2.2	1.2	3.0	0.47	0.05(3)	0.009	0.03	0.03	0.05	0.006
[Fe II] 17.94 μm	0.16	0.90	1.3	1.8	0.87	0.03(2)	0.005	0.015	0.03	0.04	0.013
[S III] 18.71 μm	0.82	5.0	5.2	2.5	4.2	0.08(2)	0.025	0.08	0.15	0.05	0.06
[O IV] 25.91 μm	2.3	13	11	12	7.2	0.20(5)	0.08	0.24	0.26	0.26	0.13
[S III] 33.48 μm	0.28	1.9	2.3	0.76	0.6	0.04(1)	0.011	0.05	0.06	0.015	0.015
[Si II] 34.81 μm	1.0	3.7	3.9	1.7	1.7	0.07(3)	0.04	0.10	0.11	0.03	0.04

Notes. The table contains data on the strongest lines only. The regions are numbered as in Hurford & Fesen (1996) with their positions shown on Figure 7. The “Average” column assumes single optical line reddening correction of 200 times. Note that the pixel sizes are different for the IRS LL ($5''.08$, $\lambda > 15 \mu\text{m}$) and SL ($1''.85$, $\lambda < 15 \mu\text{m}$) modules.

directly to constrain temperature and density of the emitting region, provided that the emitting region is uniform and physically the same for both lines comprising the ratio.

However, these assumptions are not fulfilled in the fast-moving knots for most of the line pairs and we cannot obtain emitting region parameters from, e.g., comparison of optical and infrared lines of [O III]. Even the density-sensitive ratios of two infrared lines should be interpreted carefully, as from the theoretical models it follows that their emission may be arising both in the pre-shock and post-shock regions having comparable emission measures of the order of 10^{19} cm^{-5} and temperatures of the order of $(0.5 - 2) \times 10^4 \text{ K}$, but densities different by a factor of thousand or more.

More specifically, the pre-shock photoionized region has low electron density (of the order of $100 - 250 \text{ cm}^{-3}$ in the SD-200 model) and produces lines having approximately low-density limit line ratio, and the post-shock cooling region ($n_e \approx 10^6 \text{ cm}^{-3}$) produces lines having high-density limit line ratio (i.e., corresponding level populations are determined by collisional processes). Therefore, instead of determining the density, some of the FIR line ratios determine contributions of high- and low-density regions to the total line emission.

In the following subsections we analyze the line flux ratios to infer the physical conditions and the line fluxes to estimate ionic and elemental abundances.

4.1. Information from the same ion line flux ratios

In the infrared range probed by the *Spitzer* and the ISO observatories, there are seven line pairs that can be used for plasma diagnostics and have at least one component detected. These line pairs arise in transitions between three lowest fine structure states $^3P_{0,1,2}$ in the ground p^2 and p^4 electron configurations. Out of these seven diagnostic pairs, three have both components detected ([O III], [S III] and [Ar V] lines) and four have detections of just one component ([O I], [Ne III], [Ne V] and [Ar III] lines).

Measured values of the flux ratios and the inferred physical parameters are summarized in Table 6.

4.1.1. [O III] FIR line flux ratio

The measured ratios of the far-infrared [O III] lines $I(51.81 \mu\text{m})/I(88.36 \mu\text{m})$ in different ISO spectra lie between 0.7 and 2.5 (see Table 3) with some indication of correlation between the line ratio and the optical line intensity (such correlation is observed also in the [S III] line ratio map constructed from the *Spitzer* data).

In the approximation of two emitting regions (pre-shock and post-shock) we use the following expression to determine the pre-shock PIR contribution to the total line b flux from the measured a and b line flux ratio $R = I_a/I_b$ (see Appendix B for derivation):

$$f_{\text{PIR},b} \equiv \frac{I_{\text{PIR},b}}{I_{\text{tot},b}} = \frac{R_2 - R}{R_2 - R_1}, \quad (4)$$

where $I_{\text{PIR},b}$ and $I_{\text{tot},b}$ denote photoionized region and total line b fluxes, and R_1 and R_2 denote theoretical line ratio values in the pre- and post-shock regions.

The [O III] line ratio of 2.5 observed from the rich in optical knots ISO LWS region #2 may thus be achieved only if 85% of the 88.36 μm line and 40% of the 51.81 μm line are arising in the pre-shock region. Corresponding theoretical line ratios in this case are $R_1 = 1.1$ and $R_2 = 9.7$ (see Table 6).

As shown by Sutherland & Dopita (1995), the 5007 \AA line is mostly arising in the pre-shock region. Now we have determined that this is the case also for the 88.36 μm line. This allows making one further step and using their flux ratio of $I(88.36 \mu\text{m})/I(5007 \text{ \AA}) \approx 0.10$ to estimate the pre-shock physical conditions. This line ratio is sensitive both to density and temperature and corresponds to n_e of several hundreds cm^{-3} for temperatures $(1.0 - 1.5) \times 10^4 \text{ K}$ (see Table 6), i.e., values very similar to, but somewhat different from, ones given by the SD-200 model having $T_e \approx 1.0 \times 10^4 \text{ K}$ and $n_e \approx 200 \text{ cm}^{-3}$. The constraint on the pre-shock region emitting these [O III] lines is shown on Figure 8.

4.1.2. [O I] FIR line flux ratio

It is more difficult to use the [O I] line ratio for the quantitative analysis, as only one of the lines is detected. From ISO observations of region #2 we have the 3σ lower limit on the $I(63.19 \mu\text{m})/I(145.5 \mu\text{m})$ line ratio of about 30.

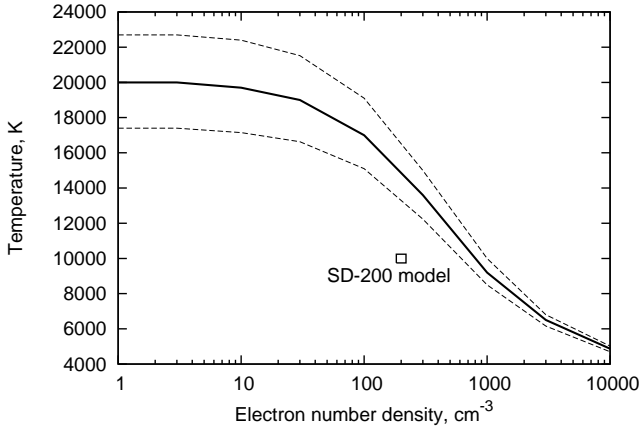
Table 6. Information from the same ion line flux ratios measured in the FMKs. See text for details.

Spectrum	line <i>a</i>	line <i>b</i>	Flux ratio	Single region		Two regions			
				T_e , K *	n_e , cm ⁻³	R_1	R_2	$f_{\text{PIR},a}$	$f_{\text{PIR},b}$
[O I]	63.19 μm	145.5 μm	> 30	< 100	any				
[O III]	51.81 μm	88.36 μm	2.5	200 – 1×10^4	$> 2 \times 10^5$	1.1	9.7	0.40	0.85
[O III]	88.36 μm	5007 \AA	0.10	$300 - 1.5 \times 10^4$	500 – 1000			1.0*	1.0*
				1.0×10^4	800			1.0*	1.0*
				1.5×10^4	200				
[Ne III]	36.01 μm	15.56 μm	< 0.08	any	any				
[Ne V]	24.32 μm	14.32 μm	< 0.2	$< 3 \times 10^4$	$> 3 \times 10^4$				
[S III]	33.48 μm	18.71 μm	0.5	$600 - 3 \times 10^4$	1500 – 3000	1.8	0.09	0.85	0.25
[Ar III]	21.83 μm	8.991 μm	< 0.10	any	any				
[Ar V]	7.914 μm	13.07 μm	1.6	$1500 - 3 \times 10^4$	$(4 - 10) \times 10^4$	1.0	6.7	0.5	0.9
[Fe II]***	1.3209 μm	1.2946 μm	0.75	any	$> 2 \times 10^5$				
[Fe II]***	1.3209 μm	17.94 μm	0.024	1700–3000**	any				
				1700–1800**	$> 1 \times 10^5$ *				

* Assumed value

** Derived value

*** The [Fe II] line flux ratios are discussed in Section 5.1.

**Fig. 8.** The constraints on the pre-shock region emitting the [O III] lines from the average $I(88.36 \mu\text{m})/I(5007 \text{\AA})$ line flux ratio (solid line). The dashed lines correspond to the constraints if the line flux ratio is changed by 20%. The square denotes the expected value based on the SD-200 model.

Some information may still be obtained from this lower limit: it corresponds either to extremely low temperatures below 100 K or high electron densities above 10^5 cm^{-3} (see Table 6).

According to the theoretical models, there is essentially no neutral oxygen in the post-shock cooling region because of slow recombination processes. The models also predict rapid ionization of neutral oxygen in the pre-shock PIR with very low line ratio $I(63.19 \mu\text{m})/I(5007 \text{\AA})$ of much less than 0.01 (the observed value is 0.07, see Table 4). The pre-shock region as the [O I] line origin is also excluded from the observed value of the $I(63.19 \mu\text{m})/I(145.5 \mu\text{m})$ line ratio.

From this we conclude that the far-infrared [O I] line emission in the FMKs arises in the dense photoionized region after the shock.

The very high values for this line flux ratio to the 5007 \AA line in the models (see Table 1) do not contradict such conclusion. Instead, the reason for these differences is the model values for

the pre-shock ion densities. For example, the Borkowski & Shull (1990) models assume very low pre-shock oxygen density of 1 cm^{-3} . Taking it higher by two orders of magnitude will decrease the post-shock 63.19 μm line intensity by a similar factor and bring the predicted intensity much closer to the results of ISO observations. The same effect will also lower the predicted 63.19 μm line intensity in Itoh (1981a,b) model that assume a pre-shock oxygen density of 30 cm^{-3} .

4.1.3. The [Ne III], [Ar III], [Ne V], [Ar V] and [S III] line flux ratios

All these lines are contained in the *Spitzer* data and, thanks to its much higher angular resolution, provide much more information for the analysis.

The upper limits on the [Ne III] and [Ar III] line ratios (see Table 6 for details on these and other line ratios) do not constrain much the plasma parameters, as both of them correspond to a wide range of densities and temperatures (Rubin et al. 2001).

Limits on the [Ne V] line ratio are also not too constraining partly because of spectral fringing near $20 \mu\text{m}$ in the IRS spectra (Ennis et al. 2006) increasing the effective noise level. Nevertheless, the limit on the [Ne V] 24.32 μm line infers that the [Ne V] emission is mostly or fully arising in the post-shock cooling region.

Similarly to the case of [O III], we have derived the fraction of the fine-structure line emission arising in the pre-shock region for [S III] and [Ar V] lines. It turns out that most of the [S III] line at 33.48 μm is arising in the pre-shock region, and we will use this fact for estimation of S abundance in the Section 4.2.

Existence of Ar^{4+} in the pre-shock region (see Table 6) is understandable, given relatively low Ar^{3+} ionization potential of 60 eV, comparable to the ionization potential of O^{2+} (55 eV). Therefore similar amounts of O^{2+} and O^{3+} in the pre-shock photoionized region in the SD-200 model give a reason to deduce that Ar^{3+} and Ar^{4+} ions also have similar number densities. Note that already Chevalier & Kirshner (1979) have shown that the visible [Ar IV] lines are arising in the low-density environment, which we associate with a pre-shock PIR.

4.2. Abundances from the flux ratios to the 5007 Å line

In general case, ionic and elemental abundances derived from the individual line intensities are strongly dependent on the theoretical model of the fast-moving knots. Such model dependence may be minimized if the spectral lines are known to be emitted in the pre-shock or the post-shock region only.

Some dependence on the underlying model still remains, but the model features used in our further analysis are relatively robust. For example, the peak of the post-shock plasma emission measure around 10^4 K is determined by the cooling rate that slows down at 2×10^4 K due to closing of the dielectronic recombination channels at lower temperatures. The low-temperature limit of the line-emitting region is computed from the upper transition level excitation energy, which is a simple but reliable estimate.

The ionic abundances in the pre-shock region are stronger dependent on the underlying model, as we estimate them for all elements from average ionization potential of the oxygen ions in the SD-200 model. Thus the pre-shock abundances may be incorrect up to a factor of several.

As follows from the theoretical models, spectral lines of singly ionized species (e.g., [Ar II], [Si II], etc.) arise mostly in the photoionized regions, whereas ones of highly-ionized species (e.g., [Ne V], [Mg V], etc.) arise mostly in the post-shock cooling regions. The only exception is the [Ar V], but the pre-shock region contribution to its lines have been already estimated above.

Below we discuss these two line groups separately and summarize the results in Tables 7 and 8.

4.2.1. High-ionization ionic species from the post-shock cooling region

An easy estimate of the plasma composition may be done if the problem is simplified by assumption of emission arising in a single layer with given temperature and electron density. In this case one can estimate relative number densities of two types of ions from their line fluxes. The line flux ratio is then expressed from Eq. (2) as

$$\frac{I_1}{I_2} = \frac{\nu_1 \varepsilon_1 n_{\text{ion},1} \Delta t_1}{\nu_2 \varepsilon_2 n_{\text{ion},2} \Delta t_2}, \quad (5)$$

where n_{ion} is ionic number density, Δt is the line emission duration in the post-shock cooling plasma element, and it is assumed that the electron densities are the same for regions emitting both lines (as it is the case in the SD-200 model). The line emissivities entering Eq. (5) are computed as described in Section 2.2.

Equation (5) may be inverted to express relative ionic abundances via the observed line ratios. In it, we always take the second line in the ratio to be the [O III] 5007 Å line.

In the following, we use the SD-200 model with the post-shock O^{2+} abundance in the line emitting region of $n(\text{O}^{2+})/n(\text{O}) \approx 1\%$. We account also for the fact that only about 2% of the total 5007 Å line emission is arising in the post-shock plasma according to the SD-200 model. This fraction is uncertain up to a factor of about two, thus introducing a systematic error of similar magnitude in all post-shock ionic abundance determinations.

There are no published results concerning theoretically predicted abundances of ions other than oxygen in the post-shock cooling region of the FMKs. To estimate them, we have utilized the electron and ion densities and the cooling function from the Sutherland & Dopita (1995) and traced the ion ionization

and recombination processes in the post-shock cooling phase using atomic data compiled by Dima Verner¹⁰ for the Cloudy code (Ferland et al. 1998).

Another source of uncertainty in the ionic abundance determination using our method are the model-dependent values of Δt , which were also computed by tracking the plasma cooling and recombination. However, calculations show that for different ions and lines the Δt values differ by no more than approximately a factor of two, that is determined by the general emission measure behavior.

Resulting model abundances are compared with the observational results in Table 7. It is seen that the abundances inferred from the SD-200 model seem to be generally consistent with the results of observations, showing that the model in general correctly represents the temperature and density evolution in the post-shock cooling region. The [Ar V] and [Ne V] lines are the only ones showing significant differences with respect to the model expectations, although the derived ionic abundances do not exceed significantly the corresponding elemental abundances.

Note that the two highest ionization fine-structure lines of [Si X] and [Si VI] observed from the fast-moving knots have not been observed by *Spitzer*, but detected in the near-infrared spectra by Gerardy & Fesen (2001). We have determined their line flux ratios to the [O III] 5007 Å line using reddening measurements from the same regions by Hurford & Fesen (1996).

4.2.2. Low-ionization ionic species from the pre-shock PIR

The post-shock plasma recombination is so much slower than the cooling, that even at $T_e \approx 300$ K the post-shock cooling plasma still mostly contains multiply-charged ions, resulting in essentially no infrared line emission from singly ionized atoms at wavelengths shorter than several tens of μm .

In this Section, we neglect any contribution to the line fluxes from the post-shock *photoionized* region. Its possible existence and physical conditions are discussed in Section 5.2.

Then we can write Eq. (2) in the form similar to Eq. (5) for the pre-shock region:

$$\frac{I_1}{I_2} = \frac{\nu_1 \varepsilon_1 n_{e,1} n_{\text{ion},1} \Delta t_1}{\nu_2 \varepsilon_2 n_{e,2} n_{\text{ion},2} \Delta t_2}. \quad (6)$$

The equation contains also the electron density ratio, as the ions having different ionization potentials exist in regions having different electron densities.

In contrast to the post-shock case, where the emission measure behavior determined approximate equality of the line emission times Δt , here the timescales are determined by the ionization rates and may vary by an order of magnitude or more from ion to ion.

From the SD-200 model we adopt the average ionization potential (IP) as a function of time and compute ionization state distribution for all elements with the simple approximation that this average IP is equal for all of them. We also take the temperature profile from the model, that has some effect on the resulting emissivities. Fortunately, exact temperature values have only minor effect on the obtained abundances, as the infrared line emissivities depend weakly on T_e above 10^3 K or so.

In the pre-shock ionization front of the SD-200 model, each initially neutral atom is consequently ionized with maximum

¹⁰ <http://www.pa.uky.edu/~verner/atom.html>

Table 7. Estimated FMK post-shock ionic abundances $n_{\text{ion}}/n_{\text{O}}$. See text for details.

Line	$I/I(5007 \text{ \AA})$	$T_e, \text{ K}$	$\epsilon, \text{ cm}^3/\text{s}$	$\Delta t, \text{ s}$	$n_{\text{ion}}/n_{\text{O}}$	$n_{\text{ion}}/n_{\text{O}} (\text{model})^*$
[Si x] 1.430 μm	0.0016	2×10^4	2.5×10^{-8}	2000	1.5×10^{-4}	2×10^{-4}
[Si vi] 1.964 μm	0.004	1×10^4	2.0×10^{-9}	2000	0.003	0.01
[Mg v] 5.608 μm	< 0.003	5×10^3	8.0×10^{-9}	2000	<0.002	0.002
[Ar v] 7.914 μm	0.005**	1×10^4	5.0×10^{-8}	2000	0.004	3×10^{-5}
[Ne v] 14.32 μm	0.015	1×10^4	2.0×10^{-9}	3000	0.08	0.002

* Estimated based on SD-200 model. The following elemental abundances are assumed to deduce the model ionic abundances with respect to oxygen: $n(\text{Ne})/n(\text{O})=0.04$, $n(\text{Mg})/n(\text{O})=0.01$, $n(\text{Si})/n(\text{O})=0.05$, $n(\text{Ar})/n(\text{O})=0.005$. These values are inferred from X-ray and optical measurements by Chevalier & Kirshner (1979); Willingale et al. (2002); Laming & Hwang (2003); Lazendic et al. (2006).

** This line is partly arising in the pre-shock region. As follows from Table 6, the post-shock region contribution is $I/I(5007 \text{ \AA}) \approx 0.0025$.

Table 8. Estimated FMK pre-shock ionic abundances $n_{\text{ion}}/n_{\text{O}}$ computed assuming that the lines are arising only in the pre-shock PIR. See text for details.

Line	$I/I(5007 \text{ \AA})$	$T_e, \text{ K}$	$n_e, \text{ cm}^{-3}$	$\epsilon, \text{ cm}^3/\text{s}$	IP, eV	$\Delta t, \text{ s}$	$n_{\text{ion}}/n(\text{O})$	$n_{\text{element}}/n(\text{O})^{**}$
[Ar ii] 6.985 μm	0.5	2.0×10^4	100	4×10^{-8}	27.6	5×10^6	1.0*	0.005
[Ar v] 13.07 μm	0.003	7000	250	8×10^{-7}	75.1	5×10^7	8×10^{-5}	0.005
[Ne ii] 12.81 μm	0.10	1.5×10^4	150	5×10^{-8}	41.0	1.4×10^7	0.06	0.04
[Fe ii] 17.94 μm	0.03	2.0×10^4	50	1.1×10^{-8}	16.2	9×10^5	5.5*	0.01
[S iii] 33.48 μm	0.04	1.5×10^4	150	3.0×10^{-7}	34.8	1×10^7	0.015	0.04
[Si ii] 34.81 μm	0.07	2.0×10^4	50	1.5×10^{-7}	16.4	1×10^6	0.7*	0.05
[O iii] 88.36 μm	0.10	1.0×10^4	200	4.0×10^{-8}	54.9	3×10^7	1.1	1.0

* Shown to arises mostly in the post-shock photoionized region; see Section 5.2.

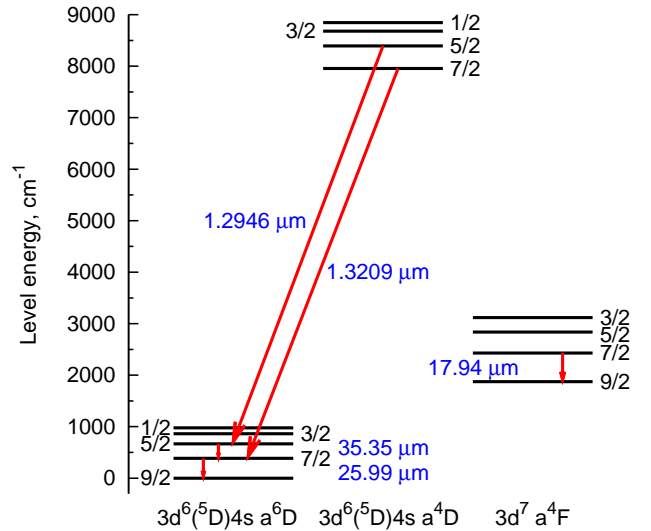
** Atomic number densities with respect to oxygen from X-ray and optical measurements by Chevalier & Kirshner (1979); Willingale et al. (2002); Laming & Hwang (2003); Lazendic et al. (2006).

ionic abundance of each ion of the order of 50-100%. Therefore the ionic abundances obtained in Table 8 should be quite close to the elemental abundances, provided that the Δt values are estimated correctly and the pre-shock PIR is giving the major contribution to the line intensity¹¹.

As a test case, we have also included in the Table 8 the similarly computed O^{2+} abundance from the [O iii] 88.36 μm line. The result is very close to the expected value of one (in fact, too close, given our uncertainties of about a factor of two), showing reliability of our method.

Although there are several [Fe ii] spectral lines in the infrared spectral range probed by *Spitzer* that originate in the low-lying electronic configurations, the two most promising are blended with other stronger lines (one at 25.99 μm is blended with [O iv] line at 25.91 μm and one at 35.35 μm is blended with [Si ii] line at 34.81 μm). Therefore in the *Spitzer* wavelength range we have used for our analysis only the [Fe ii] line at 17.94 μm (see Figure 9 for the energy levels of Fe^+ corresponding to these transitions).

From Table 8 it is seen that the Ar^+ , Si^+ and Fe^+ abundances estimated assuming that their fine-structure lines arise exclusively in the pre-shock region are much higher than the corresponding elemental abundance values obtained from optical and X-ray data (Chevalier & Kirshner 1979; Willingale et al. 2002). The possible solutions of this discrepancy are discussed in Section 5.1.

**Fig. 9.** Energy diagram of the lowest levels of Fe^+ ion with transitions used in our analysis and corresponding line wavelengths. The electron configurations are given below the diagram; numbers besides the levels denote total angular momentum J . Data from Ralchenko et al. (2007).

5. Discussion

5.1. On too high pre-shock intensities of some lines

Abundances of Ne and S derived assuming that the fine-structure lines of [Ne ii] and [S iii] are emitted in the pre-shock photoion-

¹¹ Abundance of Ar^{4+} estimated from [Ar v] lines is much lower than the Ar elemental abundance, presumably because only some fraction of Ar atoms is ionized as far as Ar^{4+} in the pre-shock region.

ized region of SD-200 model agree very well with the results of the optical and X-ray observations. Simultaneously, similarly derived abundances of other singly-charged ions (Si^+ , Ar^+ , Fe^+) are unreasonably high. They are even much higher than the respective elemental abundances obtained both from analysis of optical and X-ray spectra (Chevalier & Kirshner 1978, 1979; Willingale et al. 2002; Laming & Hwang 2003; Lazendic et al. 2006).

Within the frame of the SD-200 model, it is difficult to interpret these results and at the same time to comment on absence of other bright infrared lines, such as $[\text{Fe III}]$ line at $22.93 \mu\text{m}$ and many others.

There are several possible solutions of this mismatch between the model predictions and observations.

- The inconsistency might result from the application of the SD-200 model, describing the plasma dominated by C, O, Ne and Mg, to the plasma, containing considerable amounts of S, Si and Ar. However, total abundance of these elements with respect to oxygen reaches only 10-20% that should not significantly alter the shock structure.
- Most of fluxes in the Si and Fe infrared lines might originate in physically separated Fe-dominated clouds. This hypothesis is based on two observations:
 - (a) Cas A in the $[\text{Fe II}]$ line have different morphology than in the $[\text{O IV}]$ line (Ennis et al. 2006; Rho et al. 2008); and
 - (b) X-ray Chandra observations indicate that hot Si- and Fe-dominated blobs exist in Cas A.
 However, the Cas A morphology in the Fe $K\alpha$ X-ray line is also strongly different from morphology in the $[\text{Fe II}]$ $17.94 \mu\text{m}$ line weakening these arguments. This hypothesis could be tested by observations of the Cas A ejecta with higher spectral resolution, that would allow to determine if the $[\text{Fe II}]$ and other infrared lines from the same knots have the same peculiar velocities.
- The $[\text{Si II}]$, $[\text{Ar II}]$ and $[\text{Fe II}]$ lines might originate in separate weakly-ionized photoionized region having high emission measure. It might be situated either before the shock wave (the “far precursor” region of Itoh (1981a,b)) or after it (the post-shock PIR present in models of Itoh (1981a,b) and Borkowski & Shull (1990)). This hypothesis is further discussed below.

It is easy to distinguish between lines emitted by the pre-shock and post-shock PIRs due to their strongly different electron densities, if we use additional constraints on this line-emitting region that can be obtained from the Gerardy & Fesen (2001) observations of the near-infrared $[\text{Fe II}]$ lines (see Table 6).

The $[\text{Fe II}]$ line ratio $I(1.3209 \mu\text{m})/I(1.2946 \mu\text{m}) < 1$ indicates strongly the electron density being above 10^5 cm^{-3} at any temperature, thus weakening the hypothesis of the “far precursor”. In case of lower densities this ratio is always higher, reaching values of 10 – 20 in the low-density limit because of strong difference in the excitation rates of the respective transition upper levels (Ramsbottom et al. (2007), see Figure 9 for the transition diagram between the Fe^+ relevant levels).

Another problem for the pre-shock “far precursor” hypothesis is the observed line ratio of the $[\text{Si II}]$ $34.81 \mu\text{m}$ and $[\text{Fe II}]$ $17.94 \mu\text{m}$ lines of about 2. Both neutral and singly ionized Si and Fe atoms have similar ionization potentials, therefore we might expect that their ionization fractions are similar. Knowing the line emissivities for the low-density pre-shock PIR conditions and average abundance ratio of $n(\text{Si})/n(\text{Fe}) \approx 5$ (Willingale et al.

2002; Laming & Hwang 2003) the expected line ratio is as high as 50. We therefore conclude that the PIR contributing to the emission in these lines is likely to extend *after* the shock wave.

5.2. Post-shock photoionized region

Let us now estimate the properties of this post-shock PIR. It should not affect the optical lines of the $[\text{O II}]$ and $[\text{Fe II}]$. This sets an upper limit on this region temperature of $(5 - 10) \times 10^3 \text{ K}$. The lower limit on the temperature of about 1000 K is obtained from the requirement that the $25.99 \mu\text{m}$ $[\text{Fe II}]$ emitted by this region should not be too bright (an observational constraint is $I(25.99 \mu\text{m})/I(17.94 \mu\text{m}) < 2$).

The very low value of the near-infrared $[\text{Fe II}]$ $1.3209 \mu\text{m}$ line ratio to the $17.94 \mu\text{m}$ line corresponds to $T_e \approx 1700 \text{ K}$ in the high-density limit. However, this ratio is very sensitive to the temperature because of different excitation potentials of the transitions upper levels, so it possibly shows only the upper limit on the temperature with the near-infrared line partially arising in some smaller and slightly hotter region.

The average ionization potential should be below 20 eV, otherwise the $[\text{Ne II}]$ infrared line would be enhanced with respect to the pre-shock PIR contribution, but above 8 eV, otherwise the $[\text{Fe II}]$ and $[\text{Si II}]$ lines would not be enhanced. The average IP is probably lower than 15 eV, as the Ar should be only weakly ionized to reproduce the observed $[\text{Ar II}]$ line flux (see below). From these stringent limits it follows that silicon, sulphur and iron should be mostly singly ionized, whereas oxygen and argon are ionized only partially.

Assuming the PIR temperature of 1500 K deduced from the $[\text{Fe II}]$ line ratio, we can obtain the electron density estimates also from the limit on the FIR $[\text{O I}]$ line ratio, assuming that these lines also originate in the same region (see Section 4.1.2).

As in the case of $[\text{Fe II}]$ lines, the line ratio corresponds to $n_e \gtrsim 5 \times 10^5 \text{ cm}^{-3}$. We assume this value for the electron density and twice larger value $n_t = 1 \times 10^6 \text{ cm}^{-3}$ for the total ion density (note that in the assumption of constant post-shock pressure this corresponds to a pre-shock total ion number density of about one hundred atoms per cm^3).

Knowing plasma temperature and density, as well as the line fluxes, it is straightforward to estimate the extent of the PIR. To reproduce the $[\text{Si II}]$ line intensity with Si elemental abundance of 5% (Laming & Hwang 2003; Lazendic et al. 2006) and Si^+ ionic fraction of $n(\text{Si}^+)/n(\text{Si}) = 50\%$ the post-shock PIR should be $8 \times 10^9 \text{ cm}$ thick. This corresponds to an oxygen column density of about $8 \times 10^{15} \text{ cm}^{-2}$ that is one order of magnitude below the value obtained by Borkowski & Shull (1990) in their models.

In the post-shock region the $[\text{Si II}]$ $34.81 \mu\text{m}$ line emissivity is strongly damped due to collisional deexcitation. This allows to obtain similar values for the post-shock PIR thickness from all three remaining lines thought to be arising in it: the $[\text{Fe II}]$ $17.94 \mu\text{m}$, $[\text{Ar II}]$ $6.985 \mu\text{m}$ and $[\text{O I}]$ $63.19 \mu\text{m}$, if we take the ionic fractions of 50% for Fe^+ and O^0 and 20% for Ar^+ .

The difference between observationally derived and theoretically predicted thicknesses of the post-shock PIR may arise due to different temperature and ionization structure, as the Borkowski & Shull (1990) models describe pure oxygen plasma. For example, if the temperature falls below 100 K, emissivities of all fine-structure lines are strongly diminished. Though, in this case bright metal recombination lines are formed (Docenko & Sunyaev 2008) that are at least one order of magnitude brighter than current observational limits of optical observations of Cas A.

Another possibility is a hydrodynamical disruption of the post-shock region, like one proposed by Itoh (1986), resulting in 90% of the ionizing radiation either going through or around the post-shock region. Such disruption have been observed both in numerical simulation of the shock wave interaction with the dense interstellar clouds in supernova remnants (Patnaude & Fesen 2005) and in the laser experiments emulating such interaction (Klein et al. 2003).

In the next subsection we consider if the presence of the dust may influence the conditions in the post-shock PIR hiding somehow its larger extent.

5.3. Effects of the dust on the post-shock PIR structure

Using the data from Rho et al. (2008) it is straightforward to estimate the dust mass in each pixel of the *Spitzer* map of the Cas A. Its comparison with the optical image of this supernova remnant allows to determine the dust-to-gas mass ratio in the bright knots using the [O III] line flux predicted by the SD-200 model.

If the emitting dust with temperature $T_d \approx 100$ K (Rho et al. 2008) is distributed over all volume of the knot, then the dust-to-gas mass ratio is of the order of 2-5%. If, on the other hand, the dust is emitting only in the line-emitting regions, then this mass ratio is of the order of unity. In this case, which will be discussed further, the dust may noticeably influence the physical conditions in the post-shock region.

The dust is highly efficient energy sink decreasing the medium temperature. From the *Spitzer* spectra it is easy to estimate that the flux in the dust continuum is ten times higher than in the infrared lines (see Section 3.2.3). This may be the reason why the post-shock PIR temperature inferred from the infrared spectra is approximately twice less than the values predicted by Itoh (1981a,b) and Borkowski & Shull (1990) models.

At lower temperatures the recombination is occurring faster, resulting in shorter extent of the photoionized region and lower ionization degrees. Presence of the dust grains is also known to assist the recombination. If the ion fractions are lower by an order of magnitude than assumed above (e.g., 5% instead of 50%), then the observed size of the post-shock PIR may be reconciled with the Borkowski & Shull (1990) model predictions.

Therefore presence of large amounts of dust will diminish the post-shock PIR optical and infrared line fluxes. However, one would need to perform a more detailed analysis to understand if the quantitative agreement with the observed line-to-continuum flux ratio may be achieved without assumption of the post-shock region disruption, that was initially suggested by Itoh (1986) to explain low intensities of the neutral oxygen optical lines. Such an analysis is outside the scope of this paper.

5.4. Comparison of the model predictions with observations

As the models provide predictions only of the oxygen line relative intensities, we cannot use observations of lines of other ions for a direct comparison with the models.

Comparing observed far-infrared line ratios with theoretical model results (see Table 1), we see that the Itoh (1981a,b) models underestimate the [O III] and [O IV] line fluxes by factors of 3–40, as a result of having much lower average ionization degree after the shock wave passage than in other models. In contrast, Borkowski & Shull (1990) model BS-F and Sutherland & Dopita (1995) model SD-200 that do not account for the electron conductivity are overpredicting emission in the [O IV] line by factors of 20 – 40.

The remaining model (BS-DC of Borkowski & Shull (1990)) predicts the infrared line fluxes to within a factor of several, except for the neutral oxygen lines, but this problem is at least partially resolved by increasing the pre-shock density (see Section 4.1.2). This strongly suggests that taking into account the electron conductivity is essential for a model to reproduce the observations.

The [O III] far-infrared line ratio $I(51.81 \mu\text{m})/I(88.36 \mu\text{m})$ in the Borkowski & Shull (1990) models is significantly higher than observed (6 vs. 2.5). This discrepancy arises as they do not include emission from the pre-shock photoionized region. In the SD-200 model, in contrast, the pre-shock region dominates the [O III] infrared line emission and diminishes this infrared line flux ratio to 1.2. Therefore to reproduce the observed line ratio the pre-shock and post-shock contributions should be comparable (see also Table 6).

The model I-H is the best in description of the neutral oxygen FIR line ratio. In this model, most of the [O I] emission is arising in the post-shock PIR. The line ratio corresponds to the high-density limit, but the predicted line intensities are about 20 times stronger than observed. As mentioned in Section 4.1.2, this discrepancy may be reduced if we assume higher pre-shock atom number density than in the model (for example, 300 cm^{-3} instead of 30 cm^{-3}), as in this case the line emissivities will decrease, whereas the ionization parameter and the column density of the PIR will stay the same.

5.5. Recombination lines in the infrared range

The metal recombination lines (RLs) are another good tracer of the cold ionized plasma. Their emissivities as functions of temperature have no exponential cutoff at low T_e 's and increase with decreasing temperature approximately as T_e^{-1} at $T_e < 10^4$ K. The line emissivities are only weakly dependent on density.

However, their emissivities are 4–6 orders of magnitude less than those of the fine-structure infrared lines in the low-density limit. The infrared RL emissivity ratios to the fine-structure lines increase with electron density due to collisional effects diminishing the fine-structure line emissivities as n_e^{-1} starting from some critical density. At post-shock electron densities of 10^6 cm^{-3} the emissivity ratios are much higher (Docenko & Sunyaev 2008), but the infrared RLs are nevertheless still much less intense than the fine-structure lines.

As two examples, let us consider infrared RLs near 10 and $60 \mu\text{m}$. The brightest regions emitting RLs are the post-shock cooling and photoionized regions (due to their high emission measures $n_e^2 l$) and cold region between the photoionization front and the shock wave (due to its extremely low temperature and large extent).

Let us discuss the O I 5α recombination line at $7.45 \mu\text{m}$. It is mostly arising in the post-shock photoionized region and its strongest component emissivity of $2 \times 10^{-14} \text{ cm}^3/\text{s}$ is about 5×10^5 times less than that of the [Ar II] $6.985 \mu\text{m}$ line. Accounting for the fact that O^+ is expected to be approximately 500 times more abundant than Ar^+ , the expected recombination line flux is 1000 times less than that of the $6.985 \mu\text{m}$ line, or about 10% of the background continuum emission. Estimates show that this limit is achievable with *Spitzer* with exposure of about one hour.

Another example is a O I 11α RL at $69.03 \mu\text{m}$. Its emissivity and expected intensity is approximately 5000 times less than that of [O I] fine-structure line at $63.19 \mu\text{m}$, or about $5 \times 10^{-15} \text{ erg/cm}^2/\text{s}$ from the ISO region #2. This is approximately equal to the expected 5σ 1-hour point source sensitivity of Herschel PACS instrument (Poglitsch et al. 2006). As the

Cas A is not a point source in Herschel resolution (PACS has a $10''$ pixel size and most of the emission will be contained in 4-8 PACS pixels), one will need at least few hours to achieve the 5σ detection of this recombination line.

The recombination lines of highly-charged oxygen ions from the post-shock cooling region are expected to be about an order of magnitude dimmer than the O I RLs due to lower emission measure in the region emitting these lines.

The metal recombination line observations in the mid- and far-infrared are generally more difficult than in the optical and near-infrared due to lower line emissivities and higher background continuum emission. They are also not able to provide the information about the ion producing the spectral line, but only its electronic charge. However, such observations would allow to determine abundances of ions residing in cold regions and not producing fine-structure lines. Special emphasis should be put on the singly-charged ion lines, as their recombination lines in the optical and near-infrared ranges are split into many weak components, making them more difficult to detect (Docenko & Sunyaev 2008).

6. Conclusions

We have performed a comparison of the supernova remnant Cas A fast-moving knot infrared line intensities with the predictions of various theoretical models, that describe the FMK emission as arising in the reverse shock wave interaction with the pure-oxygen or oxygen-dominated clouds. For this comparison we have analyzed archival observational data from ISO and *Spitzer* observatories. We conclude that accounting for the electron conductivity is essential to reproduce the observed line ratios. This is the reason why the Borkowski & Shull (1990) model BS-DC provides the best description of the observed oxygen line relative fluxes, although it is only precise up to a factor of several (the [O I] lines are overpredicted because of too low pre-shock density).

This emphasizes the need for better models describing shock propagation in the oxygen-dominated plasma. In this article, many line flux ratios are derived that will help to construct such future theoretical models. Future far-infrared observations with higher sensitivity and angular resolutions will allow to obtain much more information on the fast-moving knots once the models are constructed. The infrared metal recombination lines are shown to be detectable by the planned far-infrared instruments and useful for derivation of the plasma properties.

Analysis of the infrared lines of O, Ne, Si, S, Ar and Fe ions have confirmed existence of three regions contributing to the infrared and optical line emission:

- Lines of the intermediate- and highly-charged ions arise in the post-shock rapidly cooling region (e.g., [Ne v], [Ar v], [Si vi], [Si x] lines).
- Singly-charged ions with ionization potential of the neutral species below 10 – 15 eV radiate mostly from the post-shock photo-ionized region (e.g., [O I], [Si II], [Ar II], [Fe II] lines).
- Weakly- and intermediate-charged ion lines arise in the pre-shock photoionized region as well. It gives major contribution to the emission of lines of [Ne II], [O III], [S III], [Ar v], etc.

From the observed line flux ratios it follows that the post-shock photoionized region has temperature $T_e \approx 1500$ K, electron and ions densities $n_e \approx 5 \times 10^5 \text{ cm}^{-3}$ and $n_i \approx 1 \times 10^6 \text{ cm}^{-3}$ and is approximately 1×10^{10} cm thick, assuming that Si, Ar and

Fe atoms are approximately 20%-50% ionized. This is about 10 times less than the thickness predicted in the Borkowski & Shull (1990) model.

From the detailed comparison of observed infrared line intensities with the theoretically expected values, we conclude that

- The theoretical models correctly describe the general structure of the FMKs;
- Accounting for the electron conductivity brings the BS-DC model much closer to the observed oxygen FIR line ratios to the [O III] 5007 Å line than the BS-F and SD-200 models;
- Accounting for the emission from the photoionized region before the shock front is essential to reproduce the FIR [O III] line ratio;
- The FIR [O I] line intensities in the Itoh (1981b) and Borkowski & Shull (1990) models are overestimated due to too low pre-shock atom number densities;
- The pre-shock atom number density is at least 100 cm^{-3} and may be as high as 300 cm^{-3} ;
- The post-shock photoionized region truncation, like suggested by Itoh (1986), may be needed to explain apparent thickness of the post-shock PIR being only 10% of the value predicted by the models, but effects of the dust may also be important in resolving this discrepancy.

Acknowledgements. DD is thankful to Mike Revnivtsev for many useful advices on data processing.

The version of the ISO data presented in this paper correspond to the Highly Processed Data Product (HPDP) set called 'Uniformly processed LWS L01 spectra' by C. Lloyd, M. Lerate and T. Grundy, available for public use in the ISO Data Archive, <http://www.iso.vilspa.esa.es/ida/>.

Some of the data presented in this paper were obtained from the Multimission Archive at the Space Telescope Science Institute (MAST). They are based on observations made with the NASA/ESA Hubble Space Telescope, obtained from the Data Archive at the Space Telescope Science Institute, which is operated by the Association of Universities for Research in Astronomy, Inc., under NASA contract NAS 5-26555. These observations are associated with program # 10286.

Part of this work is based on observations made with the *Spitzer* Space Telescope, which is operated by the Jet Propulsion Laboratory, California Institute of Technology under a contract with NASA. This research made use of Tiny Tim/Spitzer, developed by John Krist for the Spitzer Science Center. The Center is managed by the California Institute of Technology under a contract with NASA.

CHIANTI is a collaborative project involving the NRL (USA), RAL (UK), MSSL (UK), the Universities of Florence (Italy) and Cambridge (UK), and George Mason University (USA).

References

- Arendt, R. G., Dwek, E., & Moseley, S. H. 1999, *Astrophys. J.*, 521, 234
- Baade, W. & Minkowski, R. 1954, *Astrophys. J.*, 119, 206
- Baars, J. W. M., Genzel, R., Pauliny-Toth, I. I. K., & Witzel, A. 1977, *Astron. Astrophys.*, 61, 99
- Berrington, K. A., Saraph, H. E., & Tully, J. A. 1998, *Astron. Astrophys. Suppl. Ser.*, 129, 161
- Bieging, J. H. & Crutcher, R. M. 1986, *Astrophys. J.*, 310, 853
- Blum, R. D. & Pradhan, A. K. 1992, *Astrophys. J. Suppl. Ser.*, 80, 425
- Borkowski, K. J. & Shull, J. M. 1990, *Astrophys. J.*, 348, 169
- Butler, K. & Zeppen, C. J. 1994, *Astron. Astrophys. Suppl. Ser.*, 108, 1
- Chevalier, R. A. & Kirshner, R. P. 1978, *Astrophys. J.*, 219, 931
- Chevalier, R. A. & Kirshner, R. P. 1979, *Astrophys. J.*, 233, 154
- Delaney, T. A. 2004, PhD thesis, University of Minnesota
- Dere, K. P., Landi, E., Mason, H. E., Monsignori Fossi, B. C., & Young, P. R. 1997, *Astron. Astrophys. Suppl. Ser.*, 125, 149
- Dinerstein, H. L., Lester, D. F., Rank, D. M., Werner, M. W., & Wooden, D. H. 1987, *Astrophys. J.*, 312, 314
- Docenko, D. & Sunyaev, R. A. 2008, *ArXiv e-prints*, 0802.1911
- Dopita, M. A., Binette, L., & Tuohy, I. R. 1984, *Astrophys. J.*, 282, 142
- Dufton, P. L. & Kingston, A. E. 1991, *MNRAS*, 248, 827
- Ennis, J. A., Rudnick, L., Reach, W. T., et al. 2006, *Astrophys. J.*, 652, 376

Ferguson, J. W., Korista, K. T., & Ferland, G. J. 1997, *Astrophys. J. Suppl. Ser.*, 110, 287

Ferland, G. J., Korista, K. T., Verner, D. A., et al. 1998, *Publ. Astron. Soc. Pacific*, 110, 761

Fesen, R. A., Hammell, M. C., Morse, J., et al. 2006, *Astrophys. J.*, 645, 283

Galavis, M. E., Mendoza, C., & Zeippen, C. J. 1995, *Astron. Astrophys. Suppl. Ser.*, 111, 347

Gerardy, C. L. & Fesen, R. A. 2001, *Astron. J.*, 121, 2781

Griffin, D. C. & Badnell, N. R. 2000, *Journal of Physics B Atomic Molecular Physics*, 33, 4389

Griffin, D. C., Mitnik, D. M., & Badnell, N. R. 2001, *Journal of Physics B Atomic Molecular Physics*, 34, 4401

Gry, C., Swinyard, B., Harwood, A., et al. 2003, *The ISO Handbook, Volume III - LWS - The Long Wavelength Spectrometer, Version 2.1* (Series edited by T.G. Mueller, J.A.D.L. Blommaert, and P. Garcia-Lario. ESA SP-1262, ISBN No. 92-9092-968-5, ISSN No. 0379-6566. European Space Agency)

Hartmann, D. H., Predehl, P., Greiner, J., et al. 1997, *Nuclear Physics A*, 621, 83

Hines, D. C., Rieke, G. H., Gordon, K. D., et al. 2004, *Astrophys. J. Suppl. Ser.*, 154, 290

Hurford, A. P. & Fesen, R. A. 1996, *Astrophys. J.*, 469, 246

Itoh, H. 1981a, *Publ. Astron. Soc. Japan*, 33, 1

Itoh, H. 1981b, *Publ. Astron. Soc. Japan*, 33, 521

Itoh, H. 1986, *Publ. Astron. Soc. Japan*, 38, 717

Kamper, K. & van den Bergh, S. 1976, *Astrophys. J. Suppl. Ser.*, 32, 351

Kassim, N. E., Perley, R. A., Dwarakanath, K. S., & Erickson, W. C. 1995, *Astrophys. J.*, 455, L59

Klein, R. I., Budil, K. S., Perry, T. S., & Bach, D. R. 2003, *Astrophys. J.*, 583, 245

Laming, J. M. & Hwang, U. 2003, *Astrophys. J.*, 597, 347

Landi, E., Del Zanna, G., Young, P. R., et al. 2006, *Astrophys. J. Suppl. Ser.*, 162, 261

Lazendic, J. S., Dewey, D., Schulz, N. S., & Canizares, C. R. 2006, *Astrophys. J.*, 651, 250

Lennon, D. J. & Burke, V. M. 1994, *Astron. Astrophys. Suppl. Ser.*, 103, 273

Mazzotta, P., Mazzitelli, G., Colafrancesco, S., & Vittorio, N. 1998, *Astron. Astrophys. Suppl. Ser.*, 133, 403

Osterbrock, D. E. & Ferland, G. J. 2006, *Astrophysics of Gaseous Nebulae and Active Galactic Nuclei*, 2nd. ed. (University Science Books)

Patnaude, D. J. & Fesen, R. A. 2005, *Astrophys. J.*, 633, 240

Peimbert, M. & van den Bergh, S. 1971, *Astrophys. J.*, 167, 223

Pelan, J. & Berrington, K. A. 1995, *A&AS*, 110, 209

Poglitich, A., Waelkens, C., Bauer, O. H., et al. 2006, in *SPIE Conference, Vol. 6265, Space Telescopes and Instrumentation I: Optical, Infrared, and Millimeter*. Edited by Mather, John C.; MacEwen, Howard A.; de Graauw, Mattheus W. M.. Proceedings of the SPIE, Volume 6265, pp. 62650B (2006).

Ralchenko, Y., Jou, F.-C., Kelleher, D., et al. 2007, *National Institute of Standards and Technology, Gaithersburg, MD*

Ramsbottom, C. A., Hudson, C. E., Norrington, P. H., & Scott, M. P. 2007, *Astron. Astrophys.*, 475, 765

Reed, J. E., Hester, J. J., Fabian, A. C., & Winkler, P. F. 1995, *Astrophys. J.*, 440, 706

Rho, J., Kozasa, T., Reach, W. T., et al. 2008, *Astrophys. J.*, 673, 271

Riffel, R., Rodríguez-Ardila, A., & Pastoriza, M. G. 2006, *Astron. Astrophys.*, 457, 61

Rubin, R. H., Dufour, R. J., Geballe, T. R., et al. 2001, in *Astronomical Society of the Pacific Conference Series, Vol. 247, Spectroscopic Challenges of Photoionized Plasmas*, ed. G. Ferland & D. W. Savin, 479

Smith, J. D. T., Armus, L., Dale, D. A., et al. 2007, *Publ. Astron. Soc. Pacific*, 119, 1133

Sutherland, R. S. & Dopita, M. A. 1993, *Astrophys. J. Suppl. Ser.*, 88, 253

Sutherland, R. S. & Dopita, M. A. 1995, *Astrophys. J.*, 439, 381

Tayal, S. S. 2006, *Astrophys. J. Suppl. Ser.*, 166, 634

Tayal, S. S. & Gupta, G. P. 1999, *Astrophys. J.*, 526, 544

Thompson, R. I. 1996, *Astrophys. J.*, 459, L61+

Willingale, R., Bleeker, J. A. M., van der Heyden, K. J., Kaastra, J. S., & Vink, J. 2002, *Astron. Astrophys.*, 381, 1039

Zhang, H. L., Graziani, M., & Pradhan, A. K. 1994, *Astron. Astrophys.*, 283, 319

Zombeck, M. 2007, *Handbook of Space Astronomy and Astrophysics: Third Edition* (ISBN-10 0-521-78242-2 (HB); ISBN-13 978-0-521-78242-5 (HB)). Published by Cambridge University Press, Cambridge, UK)

Appendix A: *Spitzer* data cube PSF size estimate

As described by Smith et al. (2007), the mathematical transformations performed by the CUBISM software change the point

spread function (PSF) of the final data cube as compared to the initial PSF of the *Spitzer* IRS. This effect should be more pronounced on images having only few pixels per PSF width, such as constructed from the *Spitzer* IRS data cubes in the second order of each spectrograph module.

To determine the PSF changes induced by the data cube reconstruction, we have fit a two-dimensional Gaussian function to the shape of a point-like source 2MASS 23233176+5853204 situated in the map of the SL2 module. Such fit showed that (here x is coordinate along the individual slits and y – across them):

- The source x centroid oscillates with wavelength with amplitude of about 0.3 pixels. The y centroid stays constant to within 0.05 pixels.
- The PSFs both in x and y directions are larger than the *Spitzer* IRS true PSF, computed, e.g., by the *stinytim* software. The full width at half maximum (FWHM) in x and y directions on the spectral maps are larger than the IRS true PSF by 0.55 pixels and 0.9 pixels.

The presence of these features follows from the CUBISM algorithm description in Smith et al. (2007) paper. Although the values of the increase of PSF dimensions may seem insignificant at first, they are often comparable with the extent of the IRS true PSF (e.g., at $26\ \mu\text{m}$ the initial FWHM of the PSF is equal to 1.2 LL1 module pixel)

Not accounting for the described increase in the PSF size due to processing by the CUBISM software in our case would result in the *Spitzer* maps being seemingly more diffuse than e.g. optical maps smoothed to the IRS angular resolution.

Although we have measured these effects only in SL2 module, we assume that the same PSF broadening *in pixels* is occurring in other modules as well. This conclusion is qualitatively confirmed by visual comparison of optical maps smoothed to corresponding resolution with the data cube spectral line maps.

Appendix B: Derivation of the equation (4)

In the approximation of two homogeneous emitting regions 1 and 2 the observed line a and b flux ratio $R \equiv I_a/I_b$ may be expressed as

$$R \equiv \frac{I_a}{I_b} = \frac{I_{a,1} + I_{a,2}}{I_{b,1} + I_{b,2}} = \frac{I_{a,1}}{I_{b,1}} \frac{I_{b,1}}{I_{b,1} + I_{b,2}} + \frac{I_{a,2}}{I_{b,2}} \left(1 - \frac{I_{b,1}}{I_{b,1} + I_{b,2}} \right)$$

Denoting the line flux ratios arising in regions 1 and 2 as $R_1 \equiv I_{a,1}/I_{b,1}$ and $R_2 \equiv I_{a,2}/I_{b,2}$, and introducing the fraction of the total line b emission arising in the region 1 as

$$f_{b,1} \equiv \frac{I_{b,1}}{I_{b,1} + I_{b,2}},$$

we obtain that

$$R = R_1 f_{b,1} + R_2 (1 - f_{b,1}).$$

Expressing $f_{b,1}$ from this linear relation, we finally derive Equation (4):

$$f_{b,1} = \frac{R_2 - R}{R_2 - R_1}.$$